

# MODELING AND FLIGHT DATA ANALYSIS OF SPACECRAFT DYNAMICS WITH A LARGE SOLAR ARRAY PADDLE

Takanori Iwata\*

Japan Aerospace Exploration Agency (JAXA), Tsukuba, Ibaraki, JAPAN

Ken Maeda†

NEC Corperation, Fuchu, Tokyo, JAPAN

and

Hiroki Hoshino‡

NEC TOSHIBA Space Systems, Fuchu, Tokyo, JAPAN

## Abstract

The Advanced Land Observing Satellite (ALOS) was launched on January 24, 2006 and has been operated successfully since then. This satellite has the attitude dynamics characterized by three large flexible structures, four large moving components, and stringent attitude/pointing stability requirements. In particular, it has one of the largest solar array paddles. Presented in this paper are flight data analyses and modeling of spacecraft attitude motion induced by the large solar array paddle. On-orbit attitude dynamics was first characterized and summarized. Three characteristic motions associated with the solar array paddle were identified and assessed. These motions are the thermally induced motion, the pitch excitation by the paddle drive, and the roll excitation. The thermally induced motion and the pitch excitation by the paddle drive were modeled and simulated to verify the mechanics of the motions. The control law updates implemented to mitigate the attitude vibrations are also reported.

## 1 Introduction

On January 24, 2006, the Advanced Land Observing Satellite (ALOS) was launched by an H-IIA rocket into a sun-synchronous orbit with the altitude of 692 km (Figure 1). Since then, ALOS has been operated successfully on orbit, delivering a variety of high-resolution images in numerous quantities and contributing to disaster management support many times.

ALOS is a JAXA's flagship for high-resolution Earth observation. In order to contribute to cartography, regional environment monitoring, disaster management support, and resource survey, ALOS has three mission instruments: PRISM, AVNIR-2, and PALSAR (Figure 2).

With the mass of 4000 kg and the power of 7 kW, ALOS has the attitude dynamics characterized by three large flexible structures, four large moving components, and stringent attitude stability requirements. In particular, it has

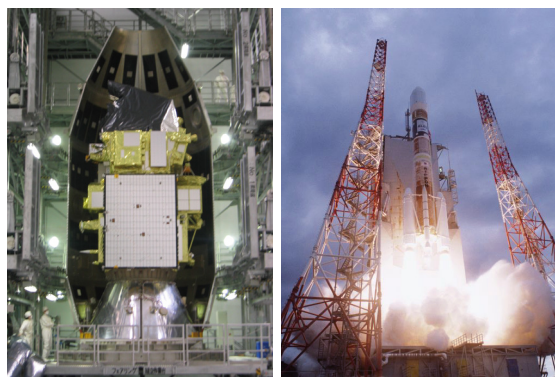


Fig. 1: ALOS Launch

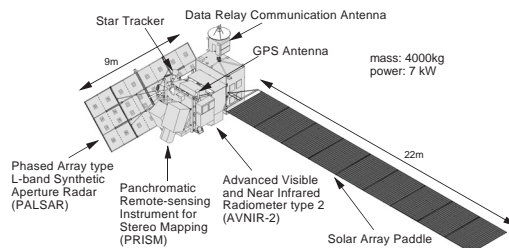


Fig. 2: ALOS On-Orbit Configuration

one of the largest single-wing solar array paddles (PDL) with the length of 23 m.

In order to provide precise geometric accuracy for globally observed high-resolution images without ground control points (GCP), ALOS is required to achieve a set of stringent pointing requirements including attitude stability ( $3.9\text{e-}4$  deg/5sec, p-p). For achieving the attitude stability requirements, a variety of platform technologies were implemented [9].

The ALOS's attitude behaviors and performances observed on orbit were assessed. The result indicated expected characteristics and unexpected characteristics. Among the characteristic motions, spacecraft dynamics coupled with the large solar array paddle dominated.

This paper presents the flight data analysis and the modeling of the paddle induced attitude motions. The

\*Ph.D., Senior Engineer, Guidance, Dynamics, and Control Engineering Group.

†Senior Manager, Space System Division.

‡Engineer, Space Systems Division.

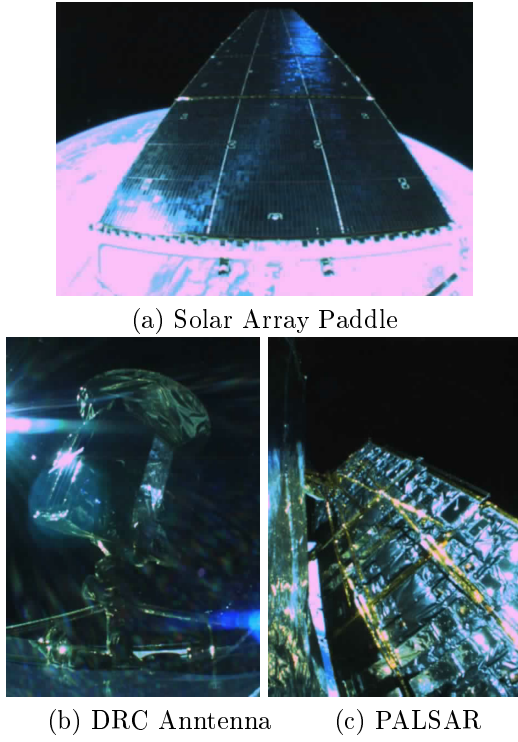


Fig. 3: Deployment Monitor Images

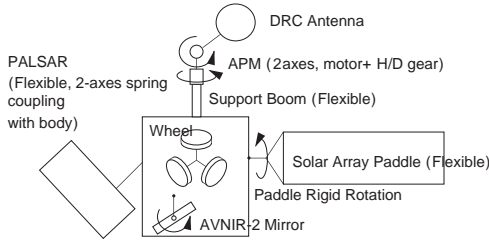


Fig. 4: Attitude Dynamics Elements

mechanism of these motions are hypothesized and verified. Control law updates implemented to mitigate the attitude vibration are also presented.

## 2 ALOS Platform Design

### 2.1 Attitude Dynamics

ALOS has three large flexible structures: a solar array paddle (PDL) with the length of 23 m, a PALSAR antenna with the length of 9 m, and a Data Relay Communication (DRC) antenna with the length of 2 m. Figure 3 presents on-orbit images of the three flexible structures captured by the ALOS's Deployment Monitors (DM) right after each deployment. The post-deployment integrity of the large flexible structures was assessed using the flight data obtained with the accelerometers and attitude sensors. Since the major low-order modes were within acceptable tolerances, we transferred the attitude control from the acquisition mode using robust thruster control to the normal mode using precision wheel control in 82 hours after the launch.

The lowest vibration modes of the flexible structures are 0.05 Hz for PDL, 0.5 Hz for PALSAR, and 3.5 Hz for DRC, in the free-free condition. Figures 4 and 5 illustrate major

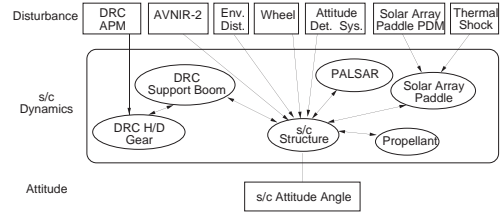


Fig. 5: Relationship of Dynamic Modes and Disturbances

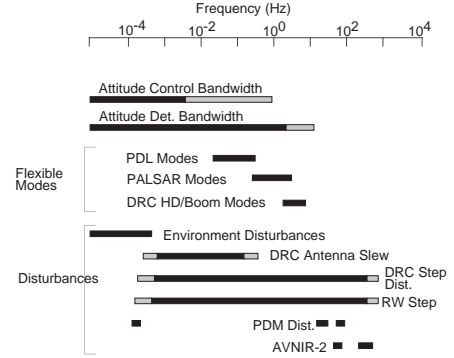


Fig. 6: Frequency Domain Characteristics of Modes and Disturbances

elements of ALOS's attitude dynamics and their relationship. Major sources of internal and external disturbances include the DRC drive, the AVNIR-2 mirror drive, the reaction wheels, the PDL drive, the PDL thermally induced motion, and the environmental disturbances. These disturbances not only affect the spacecraft rigid-body attitude, but also excite various dynamic modes of the DRC harmonic drive gear and support boom, PALSAR, PDL, the spacecraft main structure, and the propellant sloshing. Figure 6 shows the frequency domain characteristics of these modes and disturbances.

### 2.2 Solar Array Paddle

The ALOS's Solar Array Paddle (PDL) [19] is one of the largest passively deployed solar array paddles. With the on-orbit dimension of 22m and the mass of 233kg, this single wing rigid paddle has 9 panels and provides the power more than 7kW for more than 5 years. To transmit 7kW and to rotate the paddle's large moment of inertia, the ALOS's paddle drive mechanism is also the one of the largest paddle drive mechanisms.

### 2.3 Attitude and Orbit Control System

The ALOS Attitude and Orbit Control System (AOCS) [10] is a key subsystem in achieving the pointing requirements. The requirements for AOCS include the attitude control accuracy of  $\pm 0.095deg$  and the attitude stability of  $3.9e-4deg/5s$ . In order to achieve the specified accuracies, AOCS introduced a precision Star Tracker (STT), a precision GPS Receiver (GPSR), high-performance on-board computer (AOCE) based on new 64-bits space-borne MPUs, extended-Kalman-filter-based precision attitude determination and control, phase stabilization of flexible modes, precision cooperative control, and precision orbit model. The AOCS hardware



Fig. 7: ALOS Solar Array Paddle

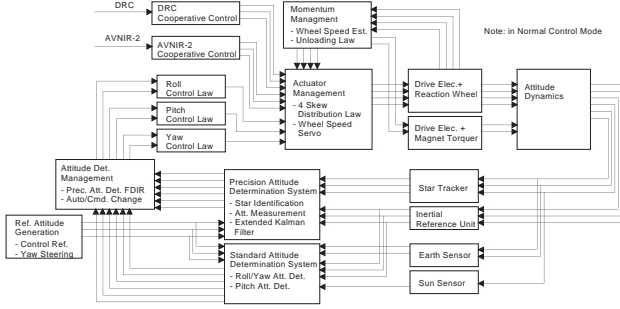


Fig. 8: AOCS Closed-Loop Block Diagram

and software are integrated to constitute the closed loop shown in Figure 8.

## 2.4 AOCS Operational Status

ALOS and its AOCS have completed its first 18 months on orbit with successful operation. All AOCS capabilities including initial acquisition mode, normal control mode, orbit control mode, and paddle sun-track control were verified on orbit. In addition, the cooperative controls for DRC, AVNIR-2, and Magnet Torquer, the DRC parameter identification, and yaw steering were verified. The STT-based precision attitude determination system have been operated continuously, and its calibration and validation have been in progress for continuous accuracy improvements.

## 2.5 Dynamics Measurements and Estimates

For the assessment of on-orbit attitude dynamics, STT measurements, Inertial Reference Unit (IRU) measurements, on-board attitude and rate estimates, more accurate ground-based attitude and rate estimates, accelerometer measurements, and Angular Displacement Sensor (ADS) measurements are available.

STT provides positions and brightness of 5 stars for each STT optical head with the star position accuracy of  $9.0\text{arcsec}$  for  $6\text{mag}$  (random error) and  $0.74\text{arcsec}$  (bias error), both in  $3\sigma$  [11]. Typically, two sets of three optical heads are used simultaneously. IRU, which is a standard unit consisting of three tuned dry gyros [10] [14], provides very accurate attitude rate for a relatively short term. Both STT and IRU are placed on the optical bench whose temperature is regulated. Attitude angles and attitude rates are estimated at  $10\text{Hz}$  by both the on-board AOCS [10] [13] and the ground-based Precision Pointing

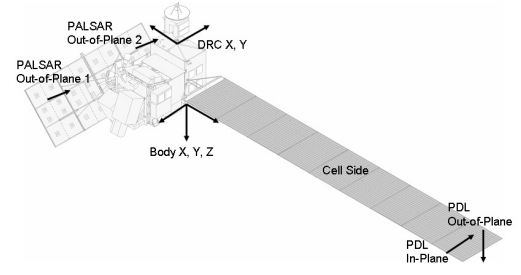


Fig. 9: Accelerometer Locations

Table 1: Attitude Control Accuracy

Condition	Axis	Attitude Control Accuracy (deg, $3\sigma$ )		
		Initial	Feedback Update~	PDL Drive Update~
No DRC Drive	Roll	$\pm 0.027$	$\pm 0.027$	$\pm 0.025$
	Pitch	$\pm 0.015$	$\pm 0.015$	$\pm 0.014$
	Yaw	$\pm 0.040$	$\pm 0.040$	$\pm 0.039$
With DRC Drive	Roll	$\pm 0.028$	$\pm 0.027$	$\pm 0.024$
	Pitch	$\pm 0.016$	$\pm 0.016$	$\pm 0.013$
	Yaw	$\pm 0.040$	$\pm 0.040$	$\pm 0.038$

and Geolocation Determination System (PPDS) [13] [14]. Flight data analyses in this paper mostly used these estimates when available. Nine low-noise accelerometers attached as in Figure 9 provide linear accelerations with  $\pm 8mG$  range at  $64\text{Hz}$  sampling [9]. Three accelerometers are for 3-axis acceleration of the body, two are for paddle out-of-plane and in-plane motions, two are for PALSAR, and two are for DRC. The 3-axis ADS installed on the optical bench can provide precise angular information ( $\pm 0.010\text{arcsec}$ , rms) from  $2\text{Hz}$  to  $500\text{Hz}$  at  $675\text{Hz}$  sampling [9] [12] [13].

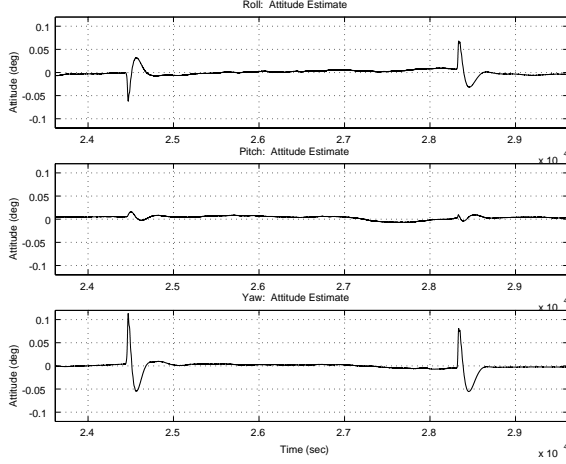
## 3 Characterization of On-Orbit Attitude Dynamics

### 3.1 Attitude Profiles

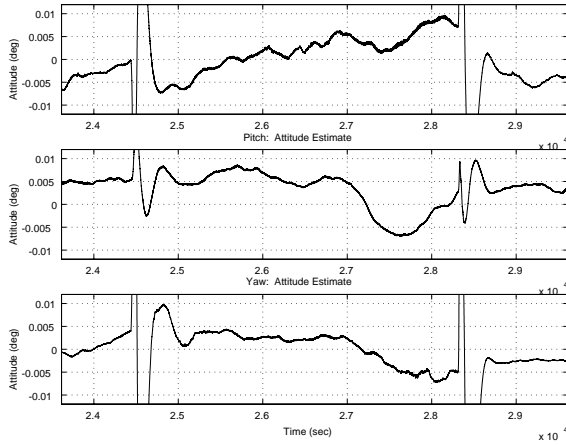
Typical estimated attitude and rate profiles over one orbit period are shown in Figures 10 and 11. These plots representing an original attitude characteristics before the control updates described later demonstrate good attitude regulation for the requirement of  $\pm 0.095\text{deg}$ . Large transient responses observed in both the attitude angles and the attitude rates at about 24500 sec and about 28300 sec are due to the thermally induced dynamics of the solar array paddle. These transient responses follow the same profiles in every orbital revolution. Larger amplitudes in attitude rates from 23750 sec to 28000 sec are induced by the tracking drive of DRC. Table 1 showed that the attitude control accuracy assessed for multiple orbital revolutions achieved  $\pm 0.040\text{deg}$ .

### 3.2 Attitude Stability Profiles

Typical attitude stability profiles for one orbit period are shown in Figure 12. Tables 2 and 3 summarize the attitude stability stochastically assessed for multiple orbit revolutions. ALOS has different attitude stability requirements for 420 sec after the initiation of the thermally induced dynamics of the solar array paddle and for the rest of the orbit period. The result indicates that ALOS meets the attitude stability requirements during the paddle's thermally induced vibration but does not meet the requirements in



(a) Full Range



(b) Narrow Range

Fig. 10: Attitude Angle Profile

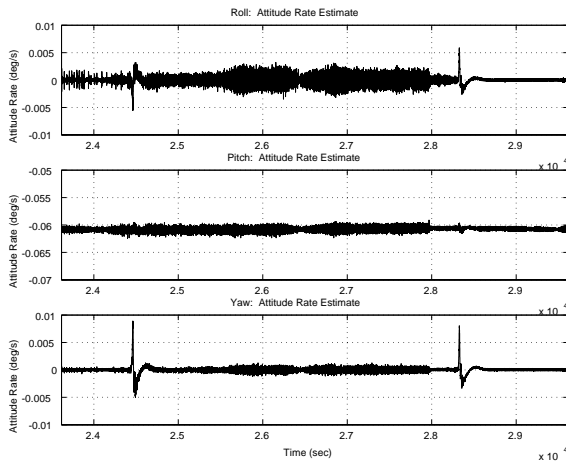


Fig. 11: Attitude Rate Profile

Table 2: Attitude Stability (excluding Eclipse Transitions)

Condition	Axis	Attitude Stability ( $deg/5sec, 3\sigma$ )		
		Initial	Feedback Update~	PDL Drive Update~
No DRC Drive	Roll	$8.8 \times 10^{-4}$	$7.7 \times 10^{-4}$	$6.1 \times 10^{-4}$
	Pitch	$5.7 \times 10^{-4}$	$6.0 \times 10^{-4}$	$3.9 \times 10^{-4}$
	Yaw	$5.1 \times 10^{-4}$	$6.2 \times 10^{-4}$	$4.8 \times 10^{-4}$
With DRC Drive	Roll	$11.5 \times 10^{-4}$	$9.9 \times 10^{-4}$	$8.2 \times 10^{-4}$
	Pitch	$6.3 \times 10^{-4}$	$6.9 \times 10^{-4}$	$5.3 \times 10^{-4}$
	Yaw	$5.9 \times 10^{-4}$	$7.2 \times 10^{-4}$	$5.3 \times 10^{-4}$

Table 3: Attitude Stability (Eclipse Transitions)

Condition	Axis	Attitude Stability ( $deg/5sec, 3\sigma$ )		
		Initial	Feedback Update~	PDL Drive Update~
No DRC Drive	Roll	0.013	0.013	0.013
	Pitch	0.0021	0.0021	0.0021
	Yaw	0.021	0.021	0.022
With DRC Drive	Roll	0.013	0.013	0.013
	Pitch	0.0021	0.0021	0.0021
	Yaw	0.021	0.021	0.022

the rest of the orbit period. A closer look at the attitude, rate, and stability profiles are shown in Figure 13.

We identified 2 major sources that violate the attitude and pointing stability requirements:

- Paddle drive (attitude and pointing stability), and
- DRC tracking drive (attitude and pointing stability).

The violation to the requirements is mainly due to a  $0.5Hz$  vibration persistently induced by the paddle drive and is secondly due to a  $0.05Hz$  vibration. In particular, the roll axis is excited significantly. In addition, the DRC tracking drive causes a  $2.5 \sim 4Hz$  vibration and degrades the attitude stability beyond its allocated budgets.

### 3.3 Frequency-Domain Characteristics

Figure 14 shows the FFT responses of attitude rate estimates for one orbit period in the normal control mode without and with DRC in drive respectively. Both frequency responses indicate the PDL's first out-of-plane mode at about  $0.05Hz$ , the PDL's second out-of-plane mode at about  $0.2Hz$ , and the PDL's first in-plane mode at about  $0.3Hz$ . At about  $0.5Hz$ , the PDL's third out-of-plane mode, its first torsional mode, and the PALSAR's first mode are observed together. At about  $1.5Hz$ , the PALSAR's third mode and the PDL's fifth out-of-plane mode are seen. The modes at around  $2.5Hz$  and around  $4Hz$  in Figure 14(b) are due to DRC, and without the DRC drive, the PSD magnitudes over  $2Hz$  were 100 times smaller than these responses. These FFT responses confirm that the major low-order modes agreed with the pre-flight analysis.

### 3.4 Characteristic Motions

Among the characteristic motions that we identified so far, the motions associated with the solar array paddle dominated the ALOS's attitude dynamics. The rest of this paper focuses on the analysis and modeling of the following three characteristic motions induced by the solar array paddle:

- Thermally induced motion of solar array paddle,
- Attitude Vibration: Pitch excitation by paddle drive, and

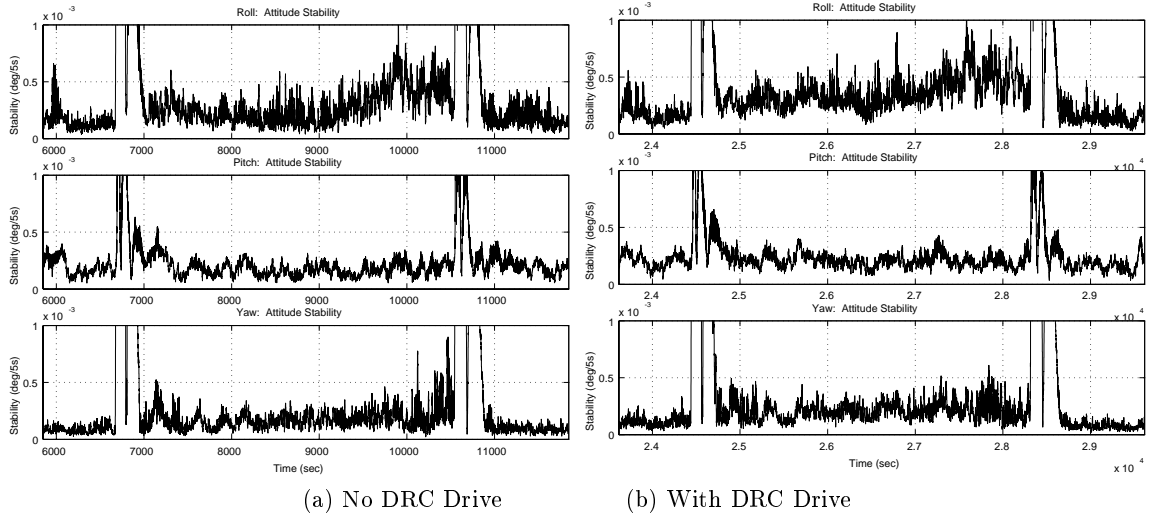


Fig. 12: Attitude Stability Profile

- Attitude Vibration: Roll excitation.

## 4 Thermally Induced Motion of Solar Array Paddle

### 4.1 Phenomena

Attitude motions thermally induced by the solar array paddle at an eclipse exit and at an eclipse entry resulted in the attitude and attitude stability profiles shown in Figures 15 and 16. The magnitude, shape, and time constant of the response repeat well from one revolution to another and they also agreed well with the pre-flight analysis [18]. At the eclipse transitions, the satellite is also subject to discontinuities in solar radiation pressure torque. However, the polarity of the motions shown in Figure 15 indicate the dominance of the thermally induced motion. The power generated by the paddle and the sun presence signal by a sun sensor on the paddle's cell side are shown in Figure 17 to indicate eclipse/day-side transitions. Figure 18 shows the temperatures on the cell side and the back side of the most inner panel and their difference. This difference is the root cause of the thermally induced motion.

### 4.2 Modeling

The thermally induced dynamics of solar array paddle was extensively modeled and experimented on the ground [17]. With the fix-free terminal condition which represents only the solar array paddle attached to a rigid wall, Reference [17] developed a detailed analytical model representing the quasi-static panel deflection and the induced dynamic vibration, and finite element models representing an experiment model and the ALOS PDL itself. The analytical model and the finite element model for the experiment were compared with the experiment results, and the comparison validated the finite element model used to predict the ALOS's on-orbit performance.

In this paper, however, a rather simple model representing coupled dynamics of attitude and solar array paddle in the free-free condition is derived to compare with the flight result. According to the notation defined in Figure 19, we obtain the following equations of motion for the satellite attitude  $\psi_b$ , the equivalent angular displacement  $\psi_s$  of the

paddle's center of mass due to the paddle's quasi-static deflection, and the equivalent angular displacement  $\psi_d$  of the paddle's center of mass due to the dynamic vibration around the quasi-static equilibrium:

$$(I_b + m_p l^2) \ddot{\psi}_b + m_p l^2 \ddot{\psi}_s + m_p l^2 \ddot{\psi}_d = T_c, \quad (1)$$

$$m_p l^2 (\ddot{\psi}_b + \ddot{\psi}_s + \ddot{\psi}_d) + c_p \dot{\psi}_d + k_p \psi_d = 0, \quad (2)$$

$$\eta_d = l \psi_d, \quad k l^2 = k_p, \quad c l^2 = c_p, \quad (3)$$

$$I_p = m_p l^2, \quad 2l = L, \quad (4)$$

$$2\zeta_p \omega_p = \frac{c_p}{I_p}, \quad \omega_p^2 = \frac{k_p}{I_p}, \quad (5)$$

where the moment of inertia of the main body is  $I_b$ , the mass of the solar array paddle is  $m_p$ , the total length of the solar array paddle is  $L$ , the control torque is  $T_c$ , the damping coefficient of the paddle's 1st out-of-plane mode is  $\zeta_p$ , and the spring constant of the paddle's 1st out-of-plane mode is  $k_p$ . If  $\psi_s(t)$  is given, these equations of motion yield the following transfer function:

$$\Psi_b(s) = \frac{-I_p^2 s^2 (2\zeta_p \omega_p s + \omega_p^2)}{I_b I_p \left[ s^2 + 2\zeta_p \omega_p \frac{I_b + I_p}{I_b} s + \omega_p^2 \frac{I_b + I_p}{I_b} \right]} \Psi_s(s) \quad (6)$$

$$+ \frac{I_p (s^2 + 2\zeta_p \omega_p s + \omega_p^2)}{I_b I_p \left[ s^2 + 2\zeta_p \omega_p \frac{I_b + I_p}{I_b} s + \omega_p^2 \frac{I_b + I_p}{I_b} \right]} T_c(s). \quad (7)$$

Based on the geometry in Figure 20, Reference [17] gives the angular displacement due to the paddle's quasi-static deformation as a function of the temperature difference between the cell side and the back side. Given the difference  $\Delta T = T_f - T_b$  between the cell-side temperature  $T_f$  and the back-side temperature  $T_b$ , the equivalent angular displacement  $\psi_s$  is obtained from

$$\Psi_s(s) = \begin{cases} -\frac{\alpha l^2}{2h} \Delta T(s) & \text{sunrise} \\ \frac{\alpha l^2}{2h} \Delta T(s) & \text{sunset,} \end{cases} \quad (8)$$

where  $\alpha$  and  $h$  are the thermal expansion ratio and the thickness of the solar array panel respectively. Finally, using Equations (6) to (8), the attitude response is

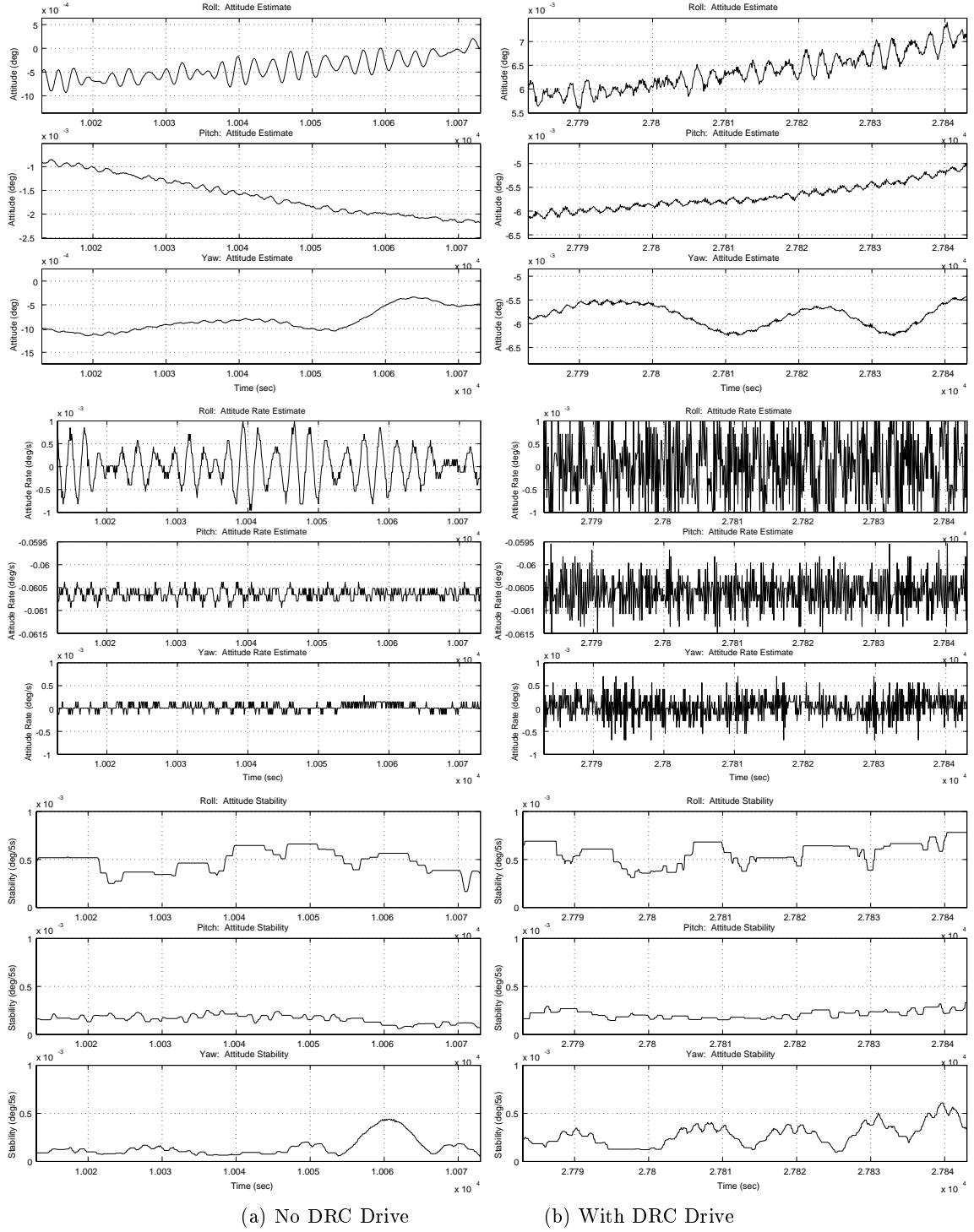


Fig. 13: Attitude Angle, Attitude Rate, and Attitude Stability

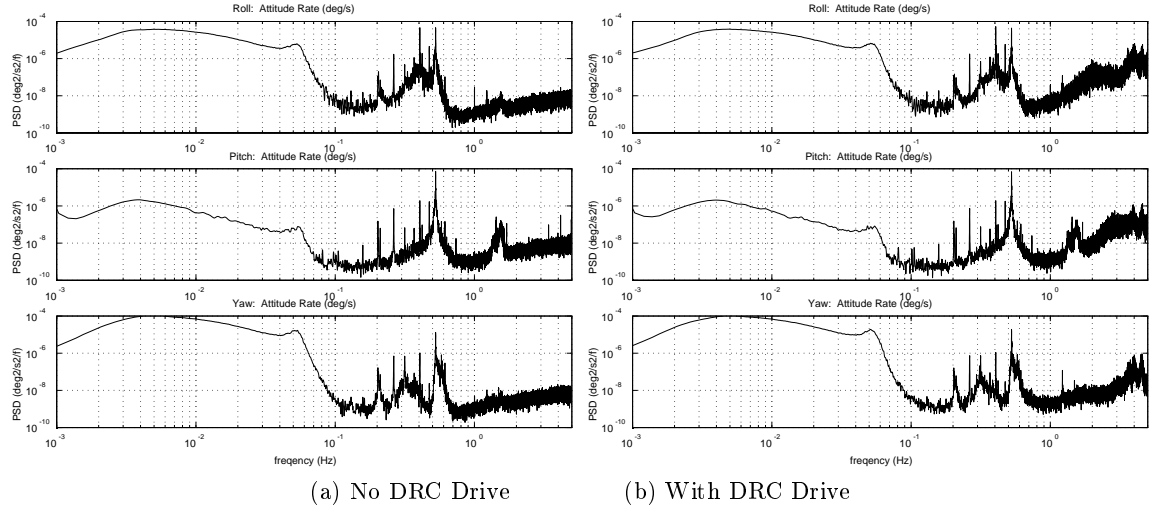


Fig. 14: Attitude Rate FFT

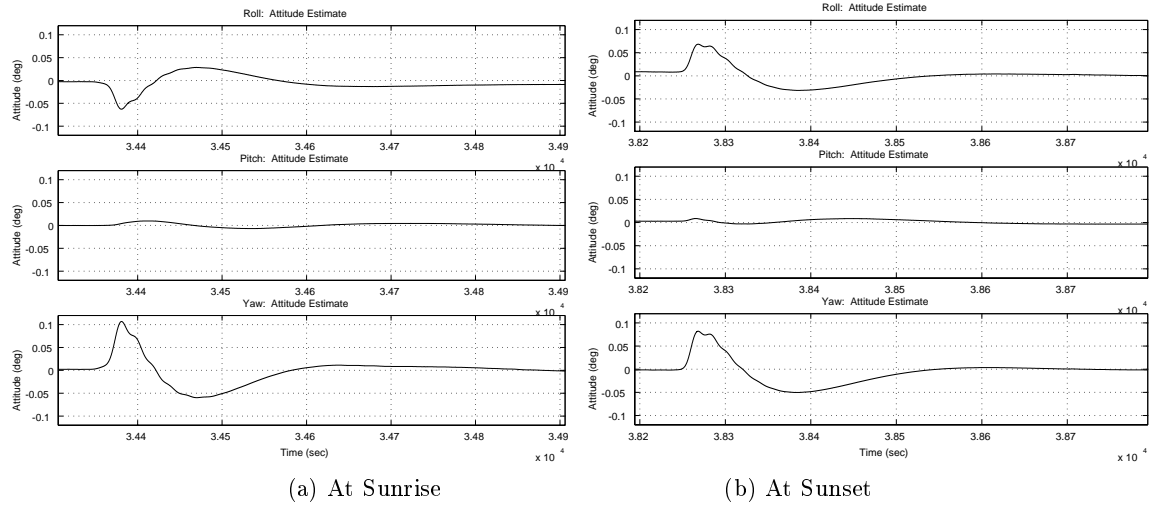


Fig. 15: Attitude Profile due to PDL's Thermally Induced Dynamics

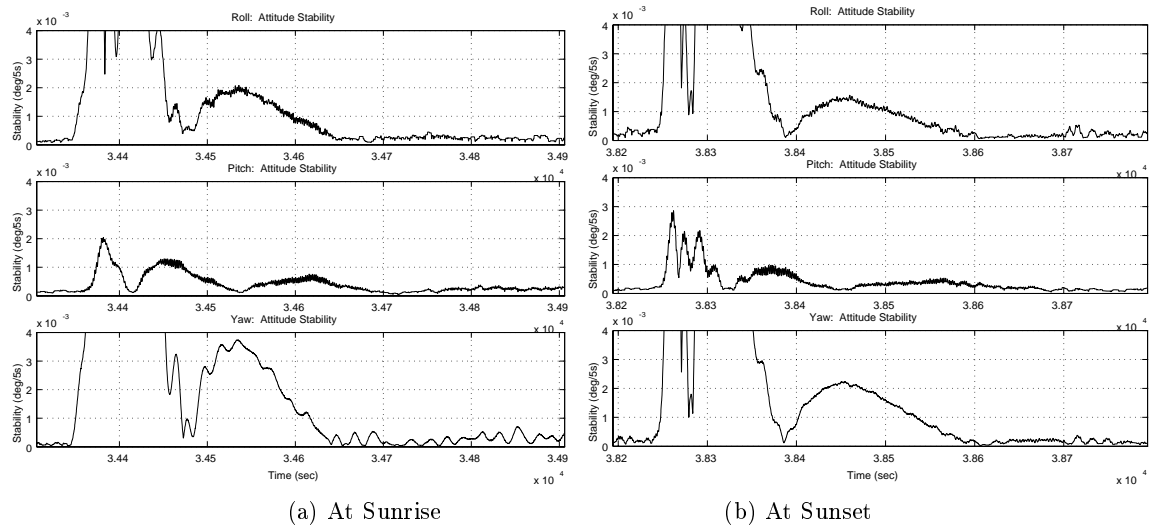


Fig. 16: Attitude Stability Profile due to PDL's Thermally Induced Dynamics

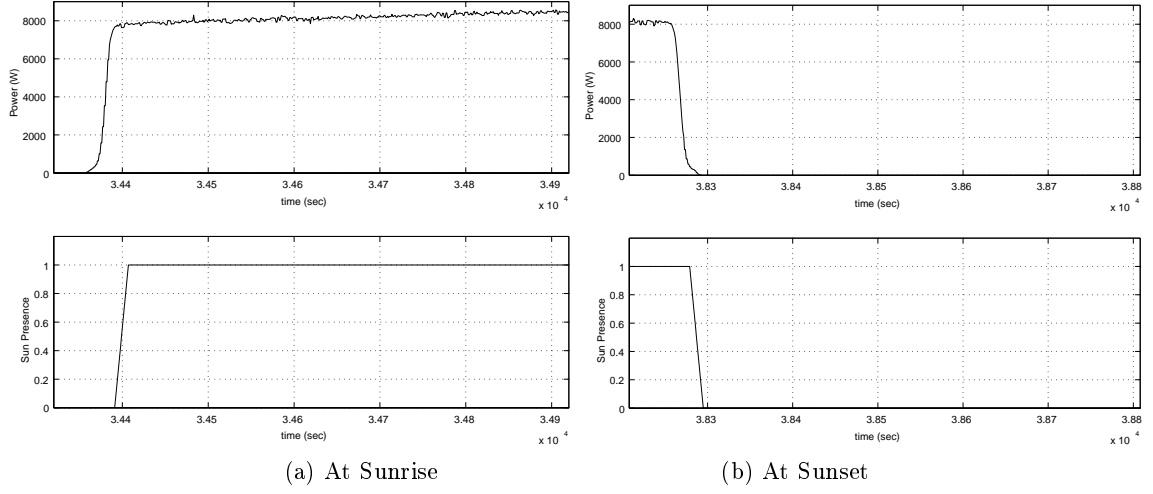


Fig. 17: Generated Power and Sun Presence at Eclipse Transitions

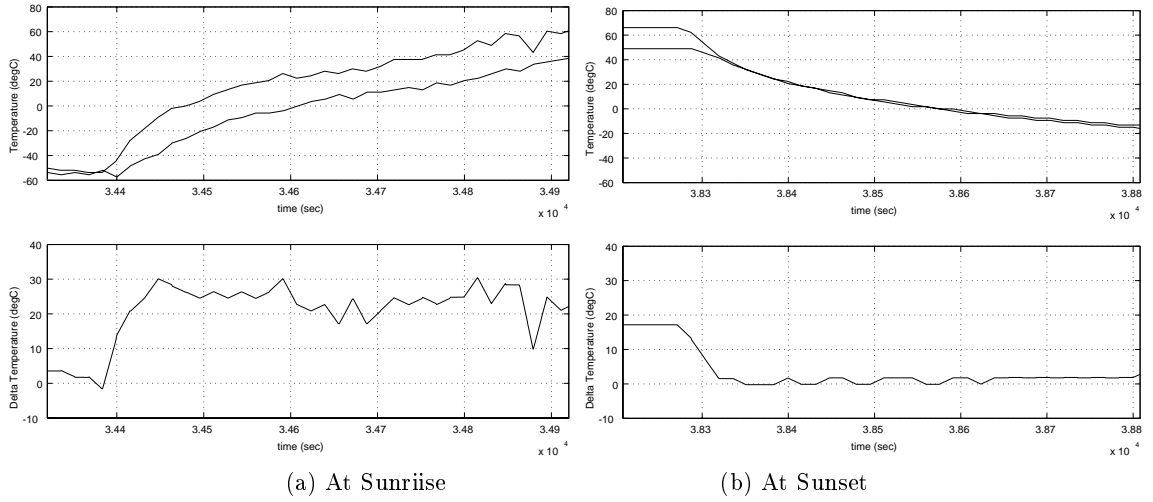


Fig. 18: PDL's Cell-Side and Back-Side Temperatures at Eclipse Transitions

obtained for a given temperature difference profile by the transfer function:

$$\Psi_b(s) = \mp \frac{-I_p^2 s^2 (2\zeta_p \omega_p s + \omega_p^2)}{I_b I_p \left[ s^2 + 2\zeta_p \omega_p \frac{I_b + I_p}{I_b} s + \omega_p^2 \frac{I_b + I_p}{I_b} \right]} \frac{\alpha l^2}{2h} \Delta T(s) \quad (9)$$

$$+ \frac{I_p (s^p + 2\zeta_p \omega_p s + \omega_p^2)}{I_b I_p \left[ s^2 + 2\zeta_p \omega_p \frac{I_b + I_p}{I_b} s + \omega_p^2 \frac{I_b + I_p}{I_b} \right]} T_c(s). \quad (10)$$

### 4.3 Analysis

Based on the on-orbit temperature telemetries shown in Figure 18, we assumed the following profile for  $\Delta T(t)$  in sunrise cases:

$$\Delta T(t) = \begin{cases} 0 & t < t_0 \\ \Delta T_0 - \Delta T_0 e^{-\frac{(t-t_0)}{\tau}} & t \geq t_0. \end{cases} \quad (11)$$

By applying this profile to the dynamics model (9) and (10) and implementing the updated feedback control law to the simulation, we obtained the attitude

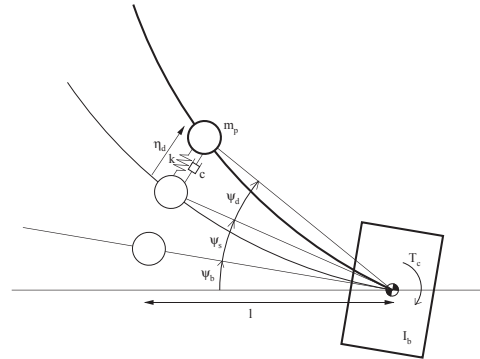


Fig. 19: Paddle's Thermally Induced Motion



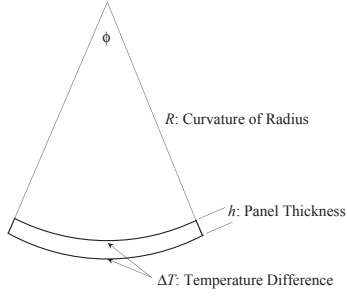


Fig. 20: Quasi-Static Deformation Geometry

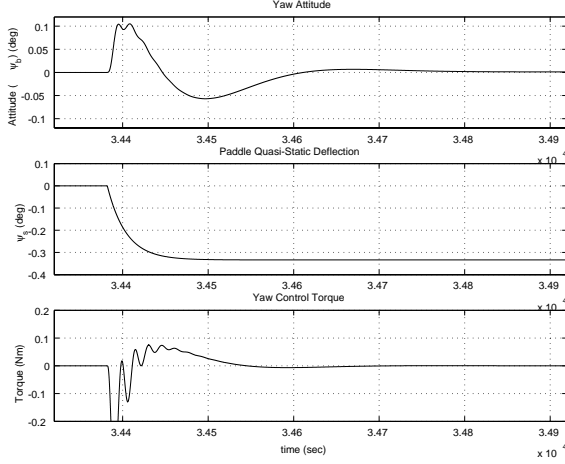


Fig. 21: Simulated Profile for PDL's Thermally Induced Dynamics (Sunrise)

profile shown in Figure 21. A comparison of this simulation result with the actual on-orbit data in Figure 15 shows an agreement in magnitude and speed of response, implying the derived model adequately represents the coupled thermally induced dynamics of attitude and solar array paddle.

## 5 Attitude Vibration: Pitch Excitation by Paddle Drive

### 5.1 Phenomena

The persistent attitude vibration observed in attitude, attitude rate, and attitude stability was typically shown in Figure 13. These plots are for the segment of argument of latitude that usually yields worst-case attitude stability. Although the vibration of  $0.5Hz$ , which coincides the paddle's torsional mode, has small amplitude, it is a dominant contributor to the degradation of attitude stability. In addition, the vibration of about  $0.05Hz$ , which seemed to be the 1st out-of-plane mode of the paddle, was observed in the yaw axis at this orbital position. These observations were confirmed by the FFT responses previously shown in Figure 14. Although the modes with these frequencies were counted in the design phase, this level of significant excitation observed on orbit were unexpected.

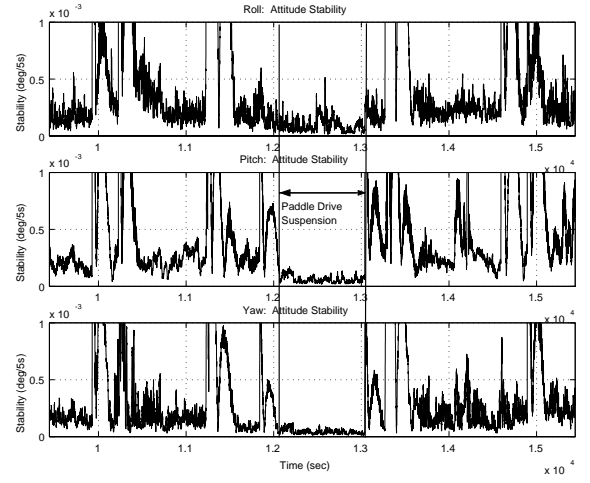


Fig. 22: Attitude Stability at Paddle Drive Suspension

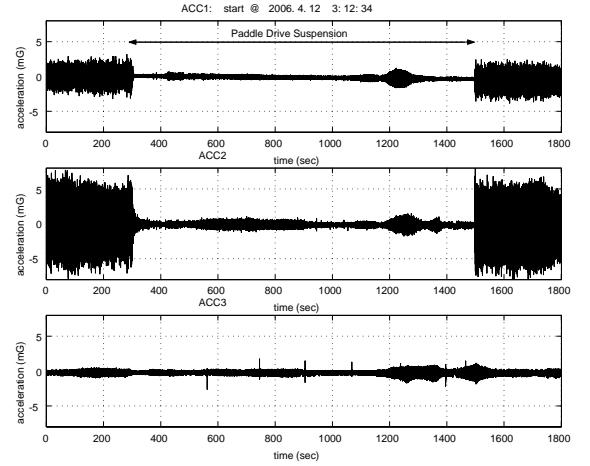


Fig. 23: Acceleration at Paddle Drive Suspension

### 5.2 Paddle Drive Suspension Experiment

In order to investigate the cause of these vibrations and to assess the effects of potential mitigation measures, we had three experimental operations: the paddle drive suspension experiment, the wheel disturbance experiment, and the paddle drive randomization suspension experiment.

Figure 22 shows the attitude stability profile obtained from the first experimental operation in which the paddle drive is temporarily suspended, and Figure 23 is the corresponding accelerometer measurements (top: paddle in-plane, middle: paddle out-of-plane, bottom: PALSAR). A detailed look at an attitude stability profile during this operation is shown in Figure 24 in comparison with a profile at the same orbit location prior to this operation. These plots clearly demonstrated that the paddle drive was a primary cause of the  $0.5Hz$  vibration and the attitude stability violation. Although due to power constraints it is not feasible to keep the paddle drive being suspended for daily operations, this 20min operation without the paddle drive resulted in the significant reduction of attitude vibration, where attitude stability values were

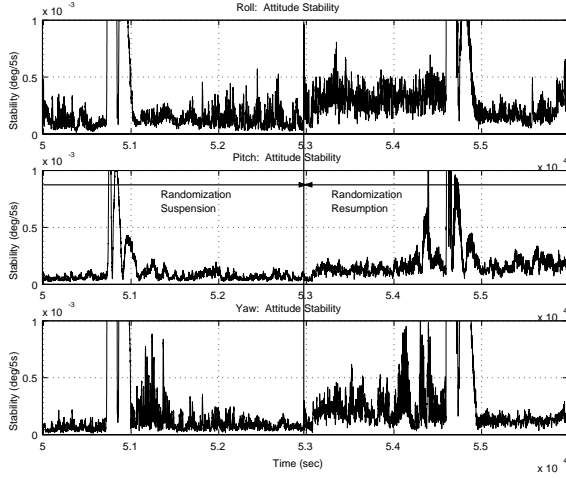


Fig. 25: Attitude Stability at Paddle Drive Randomization Suspension

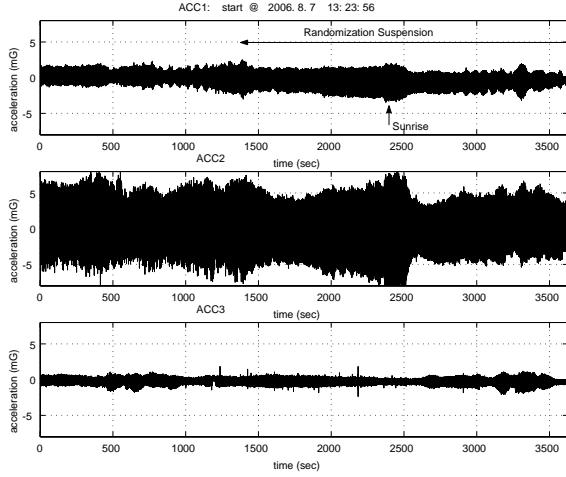


Fig. 26: Acceleration at Paddle Drive Randomization Suspension

reduced to 25 ~ 47% (Table 4).

In addition to the paddle drive suspension experiment, we had a wheel disturbance experiment to identify a source of the disturbance. The attitude, rate, and acceleration measurements obtained with the wheel bias speed setting of 0 Nms, 5 Nms, 10 Nms, 15 Nms, and 20 Nms indicated no significant change in the measurements, implying that the wheel disturbance was not a cause of the  $0.5Hz$  and  $0.05Hz$  vibrations.

### 5.3 Paddle Drive Randomization Suspension Experiment

Figure 25 shows the attitude stability profile obtained from another experimental operation without the paddle drive randomization. In order to avoid persistent excitation of structural resonances, the ALOS AOCS drives the solar array paddle with a drive pulse pattern slightly randomized instead of a fixed drive pulse pattern. The degree of the randomization, however, was

Table 4: Attitude Stability in On-Orbit Experiments

Condition		Axis	Attitude Stability (deg/5sec, $3\sigma$ )
DRC not in drive	PDL not in drive	Roll	$3.5 \times 10^{-4}$
		Pitch	$2.2 \times 10^{-4}$
		Yaw	$1.5 \times 10^{-4}$
	PDL in drive w/o randomized*	Roll	$5.1 \times 10^{-4}$
		Pitch	$2.2 \times 10^{-4}$
		Yaw	$2.5 \times 10^{-4}$

\* : during satellite noon -5 to +5 min

very limited under the constraints of the AOCS design, and the resulting pulse patterns had strong periodicity and irregularity. In the experimental operation described here, the randomization was suspended and a fixed pulse pattern of the drive rate of  $0.060deg/sec$  had been applied for about 1hour. The results were summarized in Table 4, in which the attitude stability values were reduced to 41 ~ 75% while the randomization was suspended. The reason that the randomization degraded the attitude stability instead of improving it against its design purpose is a step change of short-term drive rate with a residual periodicity of  $3 \sim 4sec$  in the randomization logic.

### 5.4 Modeling

The main cause of the persistent attitude vibration is the step motor drive and its randomization of the solar array drive. A significant difference between the on-orbit performance and a preflight analysis is due to an improper application of a step motor torque profile in an attitude stability simulation. Although the combined dynamics of step motor, harmonic drive, gear, and paddle torsional mode was properly modeled in deriving an interface torque profile, this torque profile was simplified improperly in applying the torque to satellite attitude dynamics model. Since the simplified open-loop torque profile had unrealistic equal positive and negative torque steps with higher rate, the slower  $0.5Hz$  mode was not sufficiently excited in the simulation. As the  $0.5Hz$  mode was not realistically excited, a further excitation by the randomization logic was not revealed.

We reformulated the coupled dynamics of the step motor, harmonic drive, gear, paddle torsional mode, and satellite body as described below, and confirmed the causes of the on-orbit vibration. Modeling the complex system as in Figure 28, we derive the following equations of motion:

$$\theta_1 = \theta_2, \quad (12)$$

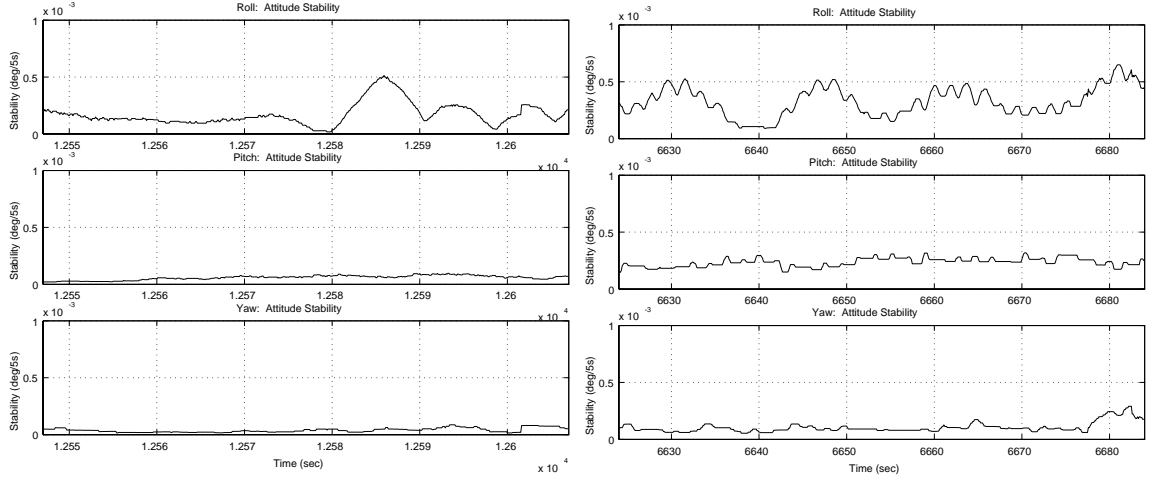
$$(J_1 + J_2)\ddot{\theta}_2 = T_1 + T_2, \quad (13)$$

$$N_h = \frac{r_3}{r_2} = -\frac{\theta_2}{\theta_3} = -\frac{T_3}{T_2}, \quad (14)$$

$$J_3\ddot{\theta}_3 - k_h(\theta_4 - \theta_3) = T_3, \quad (15)$$

$$J_4\ddot{\theta}_4 - k_h(\theta_4 - \theta_3) = T_4, \quad (16)$$

$$N_g = \frac{r_5}{r_4} = -\frac{\theta_4}{\theta_5} = -\frac{T_5}{T_4}, \quad (17)$$

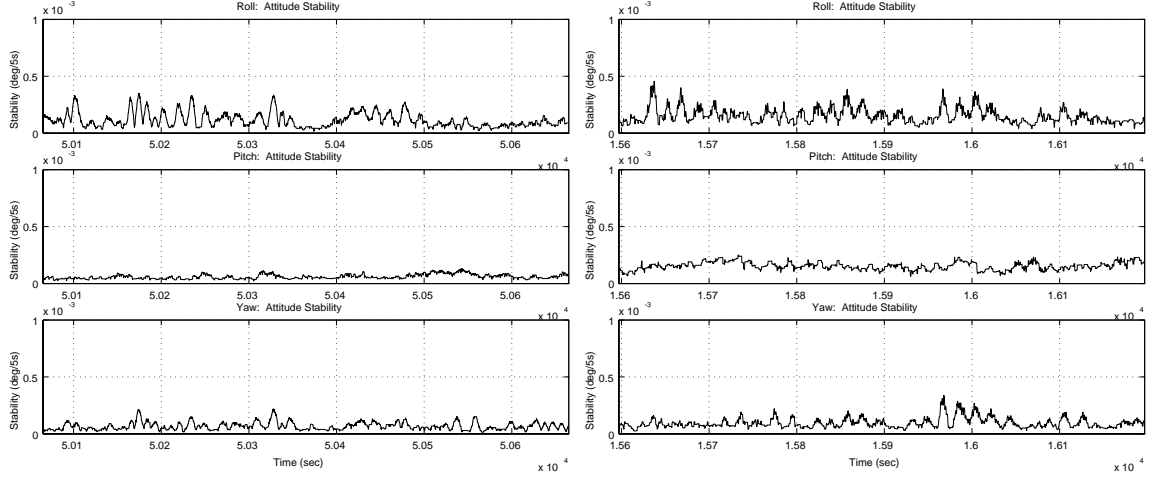


(a) During Drive Suspension

(b) With Normal Drive

\*80 sec. to 140 sec. past ascending node

Fig. 24: Attitude Stability Comparison (Close Look)



(a) During Randomization Suspension

(b) With Normal Drive

\*6 min. to 16 min. past eclipse center

Fig. 27: Attitude Stability Comparison (Close Look)

$$J_5 \ddot{\theta}_5 - c_p(\dot{\theta}_y - \dot{\theta}_5) - k_p(\theta_6 - \theta_5) = T_5, \quad (18)$$

$$J_6 \ddot{\theta}_6 + k_p(\theta_6 - \theta_5) = 0, \quad (19)$$

$$I_y \ddot{\theta}_y = T_r, \quad (20)$$

$$T_r = -\dot{H}_p, \quad (21)$$

$$H_p = (J_1 + J_2)\dot{\theta}_2 + J_3\dot{\theta}_3 + J_4\dot{\theta}_4 + J_5\dot{\theta}_5 + J_6\dot{\theta}_6. \quad (22)$$

By eliminating  $\theta_3$ ,  $\theta_5$ ,  $T_2 \sim T_5$ , and  $T_r$ , obtain the following 8th-order equations of motion:

$$\ddot{\theta}_2 = a_{21}\theta_2 + a_{23}\theta_4 + b_2T_m, \quad (23)$$

$$\ddot{\theta}_4 = a_{41}\theta_2 + a_{43}\theta_4 + a_{44}\dot{\theta}_4 + a_{46}\dot{\theta}_6 + a_{48}\dot{\theta}_y, \quad (24)$$

$$\ddot{\theta}_6 = a_{63}\theta_4 + a_{65}\theta_6, \quad (25)$$

$$\ddot{\theta}_y = a_{81}\theta_2 + a_{83}\theta_4 + a_{84}\dot{\theta}_4 + a_{85}\dot{\theta}_6 + a_{88}\dot{\theta}_y + b_8T_m, \quad (26)$$

where  $a_{ij}$  are constant parameters. In order to drive this set of equations of motion, we simulated the step motor drive mechanism as modeled in Figure 29.

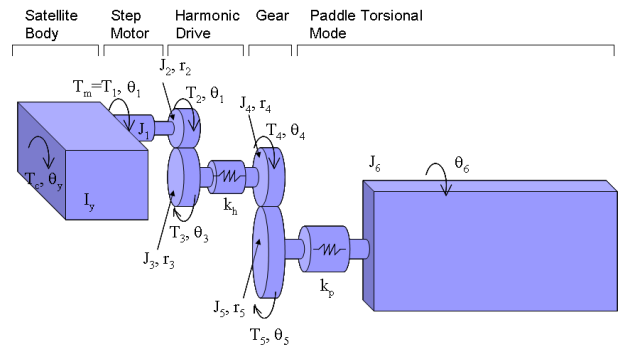


Fig. 28: Paddle Drive Dynamics

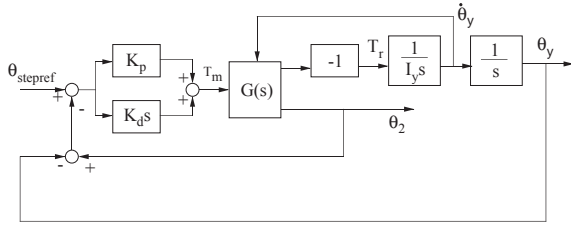


Fig. 29: PDM Drive Model

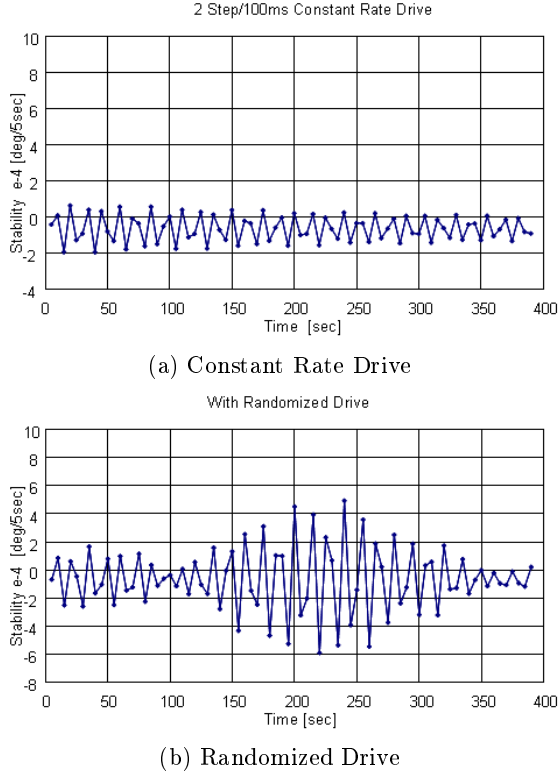


Fig. 30: Simulated Attitude Stability

Using the model developed here, the pitch attitude dynamics disturbed by the paddle's drive was simulated and the attitude stability was reexamined. We present two cases: (1) paddle driven at constant rate (2 pulses per 100 ms) and (2) paddle driven with randomization logic. The first case represents the vibration induced by the pure coupled dynamics of the step motor, harmonic drive, gear, paddle torsional mode, and satellite body. This also corresponds to the paddle drive examined by the paddle drive randomization suspension experiment. The second case represents the additional vibration induced by the randomization logic. This case corresponds to the daily operations with the original paddle drive logic. Figure 30 verified that the current paddle drive mechanism with the coupled paddle-body dynamics was indeed the main source of the pitch excitation and the randomization logic worsened the excitation. The FFT of these time-domain responses are shown in Figure 31. This frequency-domain plot suggests that the randomization logic resulted in the broader distribution of the resonance without reducing its peak.

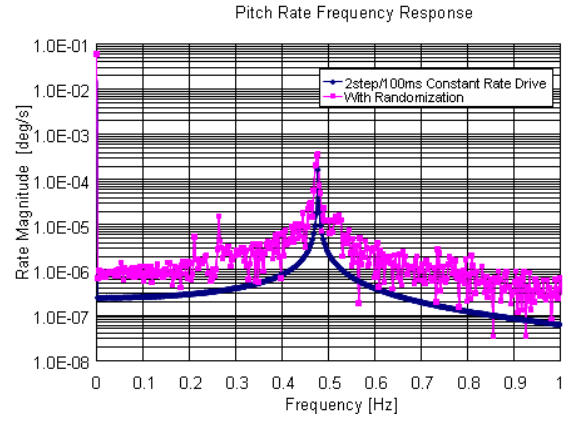


Fig. 31: Frequency Domain Comparison of Constant Rate Drive and Randomized Drive

## 5.5 Control Law Updates: Feedback Control Law

In order to improve attitude stability against the 0.5 Hz vibration, the AOCs feedback control law in the normal control mode was tuned up and upgraded on May 14, 2006. This control law update for 3 axes provides additional phase margins for the 0.5 Hz mode at the expense of gain margins for higher flexible modes and resulted in about 20% improvement in attitude stability (Table 2).

## 5.6 Control Law Updates: Paddle Drive Law

On April 20, 2007, we reprogrammed the attitude control software to update the paddle drive control logic. The updated control logic drives the solar array paddle without the randomization during the dayside of the orbit to minimize the attitude vibrations' effect on the radiometers' image. An increased sun-track error due to the constant rate drive without the randomization is compensated by the paddle track control with the randomization during the eclipse. The updated attitude stability was evaluated and the expected performance improvement was achieved.

Figure 32 presents a typical attitude stability response after the paddle drive law update. Figure 33 shows a closer look at the attitude, rate, and stability profiles in this orbit revolution. Comparisons with Figures 12 and 13 indicate improved stability and disturbance performance. The performance improvement was quantitatively assessed for multiple revolutions in Table 2.

## 6 Attitude Vibration: Roll Excitation

We have observed two types of roll excitations: the persistent vibration of about 0.5 Hz, and the intermittent vibration of about 0.5 Hz. These vibrations are partially induced by the paddle drive, but they are not entirely due to the paddle drive. This can be seen at the paddle drive suspension experiment in Figure 24, where the 0.05 Hz mode was excited in

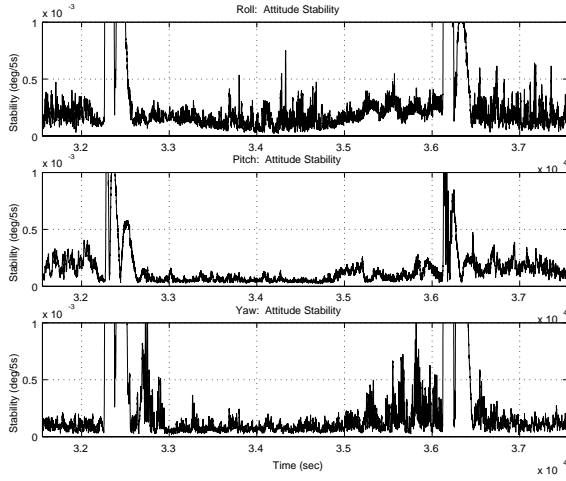


Fig. 32: Attitude Stability Profile after Paddle Drive Law Update

roll even though the paddle drive was completely suspended. The magnitudes of these vibrations depend on the orbital location and/or satellite configuration (*e.g.*, paddle's rotation angle, DRC's pointing angle). This dependency is asymmetric with respect to the orbit revolutions. Typically, the roll excitations become most significant at the dayside passage over the souther hemisphere. In particular, the region before and over the Antarctica gives the worst attitude stability. The causes of these phenomena are unknown and are currently under study. Working hypotheses include step drag torque by nonuniform upper rarefield atmosphere, cross-axes dynamic coupling, and PAL-SAR's vibration and thermally induced dynamics.

## 7 Conclusions

ALOS and its AOCS have completed its first 19 months on orbit with successful operations. All capabilities and most performances of the ALOS AOCS were verified. The ALOS attitude dynamics on orbit were characterized and analyzed with flight data. In particular, three characteristic motions associated with the solar array paddle were identified and assessed. These motions are the thermally induced motion, the pitch excitation by the paddle drive, and the roll excitation. The thermally induced motion and the pitch excitation by the paddle drive were modeled and simulated to verify the mechanics of the motions. The control law updates implemented to mitigate the attitude vibrations are also reported.

## References

- [1] Takanori Iwata, *Sensing and Control in High-Resolution Earth Observation Satellites: Present and Prospects for the 21st Century*, Measurement and Control, Vol. 40, No. 1, pp. 113–121, 2001(in Japanese).
- [2] J. Sudey, Jr. et. al., *In-Orbit Measurements of Landsat-4 Thematic Mapper Dynamic Disturbances*, Acta Astronautica, Vol.12, No.7/8, pp.485–503, 1985.
- [3] Stanley E. Woodard et. al., *Experimental Investigation of Spacecraft In-Flight Disturbances and Dynamic Response*, J. of Spacecraft and Rockets, Vol.34, No.2, 1997.
- [4] John D. Johnston and Earl A. Thornton, *Thermally Induced Dynamics of Satellite Solar Panels*, J. of Spacecraft and Rockets, Vol.37, No.5, 2000.

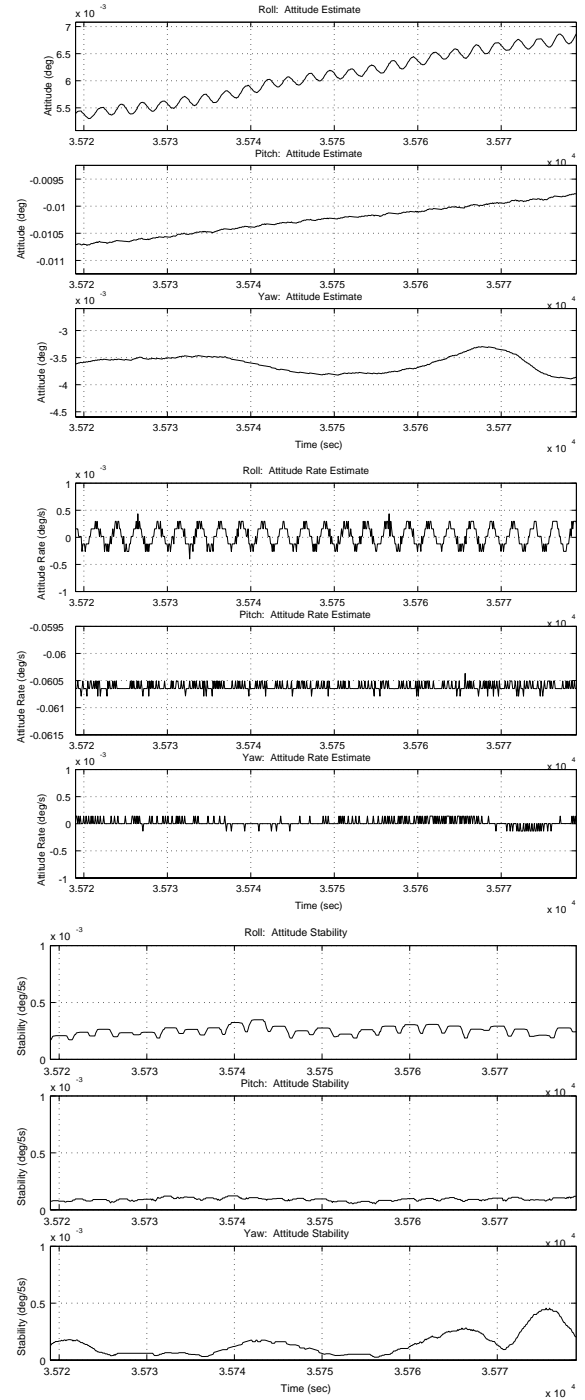


Fig. 33: Attitude Angle, Attitude Rate, and Attitude Stability after Paddle Drive Law Update

- [5] G. M. Connell and V. Chobotov, *Possible Effects of Boom Flutter on the Attitude Dynamics of the OVI-10 Satellite*, J. of Spacecraft, Vol.6, No.1, 1969.
- [6] Stanley E. Woodard, *Orbital and Configuration Influences on Spacecraft Dynamic Response*, J. of Spacecraft and Rockets, Vol.35, No.2, 1998.
- [7] Darrell F. Zimbelman, *Thermal Elastic Shock and Its Effect on TOPEX Spacecraft Attitude Control*, AAS 91-056, 1991.
- [8] Christian M. Harris et. al., *Effect of Thermal Radiation Torques on the TDRS Spacecraft*, AIAA-90-3492-CP, 1990.
- [9] Takanori Iwata, et. al., *Precision Pointing Management for the Advanced Land Observing Satellite (ALOS)*, 23rd ISTS, ISTS 2002-d-56, Matsue, Japan, 2002.
- [10] Takanori Iwata, et. al., *Precision Attitude and Orbit Control System for the Advanced Land Observing Satellite (ALOS)*, AIAA Guidance, Navigation, and Control Conference, AIAA-2003-5783, Austin, U.S.A., 2003.
- [11] Takanori Iwata, et. al., *Precision Star Tracker for the Advanced Land Observing Satellite (ALOS)*, 27th Annual AAS Guidance and Control Conference, AAS04-027, Breckenridge, U.S.A., 2004.
- [12] Takanori Iwata, et. al., *High-Bandwidth Pointing Determination for the Advanced Land Observing Satellite (ALOS)*, 24th ISTS, ISTS 2004-d-10, Miyazaki, Japan, 2004.
- [13] Takanori Iwata, *Precision Attitude and Position Determination for the Advanced Land Observing Satellite (ALOS)*, SPIE 4th International Asia-Pacific Environmental Remote Sensing Symposium, Honolulu, U.S.A., 2004.
- [14] Takanori Iwata, *Ground-Based Precision Attitude Determination for the Advanced Land Observing Satellite (ALOS)*, 25th ISTS, ISTS 2006-d-32, Kanazawa, Japan, 2006.
- [15] Takanori Iwata et. al., *Precision Attitude Determination and Control for the Advanced Land Observing Satellite (ALOS): Flight Results*, 50th Space Science and Technology Joint Conference, 06-1D05, Kitakyushu, Japan, 2006(in Japanese).
- [16] Takanori Iwata, *Advanced Land Observing Satellite (ALOS): On-Orbit Status and Platform Calibration*, IEEE International Geoscience and Remote Sensing Symposium 2007, Barcelona, Spain, 2007.
- [17] Takanori Iwata et. al., *Thermally Induced Dynamics of Solar Array Paddle: Experimental Study*, 48th Space Science and Technology Joint Conference, 1E07, Fukui, Japan, 2004 (in Japanese).
- [18] Takanori Iwata et. al., *Attitude Dynamics for the Advanced Land Observing Satellite (ALOS): Flight Results*, Proceedings of the 16th Workshop on Astrodynamics and Flight Mechanics, ISAS, Sagamihara, Japan, 2006.
- [19] Takanori Iwata et. al., *Large Solar Array Paddle System for the Advanced Land Observing Satellite (ALOS)*, 46th Space Science and Technology Joint Conference, 2E7, Koganei, Japan, 2002 (in Japanese).